Mineralogical Magazine, April 2018, Vol. 82(2), pp. 413–431

An application of the Rietveld refinement method to the mineralogy of a bauxite-bearing regolith in the Lower Amazon

Leonardo Boiadeiro Ayres Negrão[1,*], Marcondes Lima da Costa[1], Herbert Pöllmann[2] and Axel Horn[2]

[1] Instituto de Geociências, Universidade Federal do Pará, Belém-PA, Brazil
[2] Institut für Geowissenschaften und Geographie, Martin-Luther-Universität Halle-Wittenberg, Halle (Saale), Germany

[*Received 29 August 2016; Accepted 3 July 2017; Associate Editor: Karen Hudson-Edwards*]

Abstract

A comparison of Rietveld refinement results for a bauxite-bearing regolith and its clayey cover in the Amazon region was made with stoichiometric calculations from chemical analysis and partly from thermogravimetric results. For this investigation a profile in the bauxite-bearing regolith occurrence in the ALCOA bauxite mine at Juruti, Brazil was studied. The different minerals, their compositions and their low crystallinity in the different horizons were investigated and the contents determined. It is evident that some minerals show several generations and some chemical composition changes that must be included in the Rietveld refinement. Al-rich hematites and goethites are common along the bauxite profile. Amorphous contents were determined with rutile added as an internal standard and shown to have gibbsite- or kaolinite-like composition. The minerals could be quantified in the different horizons and the difficulties were mainly related to variable crystalline aspects of the phases. Rietveld refinement can be a powerful tool in bauxite prospecting, quality control and during mining and beneficiation of ore minerals using the adapted refinement strategies.

Keywords: Rietveld, bauxite, mineralogy, powder X-ray diffraction, Amazon.

Introduction

Bauxites are rocks enriched in aluminum hydroxide minerals, such as gibbsite, böhmite and diaspore, formed in humid tropical to subtropical climates from the weathering of aluminosilicate-rich parent rocks (Bárdossy and Aleva, 1990). Bauxite resources are estimated to be 55 to 75 billion tons, with reserves in Africa (32%), Oceania (23%), South America and the Caribbean (21%) and Asia (18%) (Bray, 2016). Brazil has the third largest reserves of this ore (2.6 billion tons), after Australia (6.2) and Guinea (7.4), and is the third largest producer with an estimated amount of 35 million tons of bauxite mined in 2015 (Bray, 2016). Around 97% of the Brazilian reserves are concentrated in the Amazon region, mostly on siliciclastic rocks (Lucas, 1997). Such reserves constitute important deposits, some in operation, as at Trombetas, Juruti and Paragominas (Costa *et al.*, 2014) with others under investigation such as at Rondon do Pará (Oliveira *et al.,* 2016).

The main restriction on bauxite mining in the Amazon region is the up to 25 m thick overburden made of yellowish clays, known as Belterra clay (Sombroek, 1966), along with the difficult and costly chemical and mineralogical quantification of bauxites, particularly for determining available alumina and reactive silica using traditional wet chemistry methods. Those methods are relatively slow, require large amounts of chemical reagents and considerable space and handwork (Feret, 2013).

Rietveld refinement (Rietveld, 1969) using powder X-ray diffraction is considered a practical, fast and less expensive technique when compared to mineral quantification by traditional methods, and so has been an alternative route towards bauxite's mineralogical quantification. The

*E-mail: boiadeiro.negrao@gmail.com
https://doi.org/10.1180/minmag.2017.081.056

Copyright © Mineralogical Society of Great Britain and Ireland 2018

refinement also provides crystal information to evaluate solid solutions, such as the Al-for-Fe substitutions in goethite and hematite, contributing to a better understanding of the chemical and micro-textural aspects observed in the Al-rich ore.

The bauxite deposit of Juruti is located in the Lower Amazon region (Fig. 1), in the northwest portion of the State of Pará, Brazil, ~200 km west of the city of Santarém, on the right bank of the Amazon River. Within the Juruti's ALCOA mine district, a bauxite-bearing regolith is exposed in a mining trench at the Capiranga Plateau (Fig. 1). The bauxites of Juruti developed on sedimentary rocks of the Cretaceous Alter-do-Chão formation (Costa *et al.,* 2014), representing the deposition of continental sequences terminating sedimentation in the Amazon Basin (Silva *et al.,* 2003). Like most lateritic profiles in the Amazon, the bauxites of Juruti were formed in the Paleocene–Eocene with a new bauxitization phase in the Miocene, responsible for the yellowish clay cover (Belterra clay) formation, about 6–10 Ma ago (Costa *et al.,* 2014).

The bauxite-bearing regolith, 23 m in depth (Fig. 1*d*), comprises a mottled horizon at the bottom with kaolinite, quartz and hematite; a central bauxitic horizon consisting mainly of gibbsite with kaolinite, hematite and anatase in minor proportions; an iron crust with dominant hematite and goethite; a horizon with ferruginous nodules and clayey matrix composed of hematite, goethite, gibbsite and kaolinite; a horizon with bauxitic nodules and clayey matrix where gibbsite turns into the dominant phase; and a clay cover horizon comprised mainly of kaolinite and goethite, with gibbsite, anatase and quartz in minor proportions.

Materials and methods

Thirteen samples were selected from a complete bauxite regolith and its clay overburden in the mine district of Juruti, studied previously by Cruz (2011) and Costa *et al.* (2014). The samples were described and studied under optical microscope, scanning electron microscope (SEM), X-ray fluorescence (XRF), powder X-ray diffraction (XRD) and thermal analysis. The analyses were made partly in the Institute of Geosciences of the Universidade Federal do Pará in Belém, Brazil, and in the mineralogical laboratories of the Martin-Luther-University Halle-Wittenberg in Halle, Germany. A Zeiss AXIOLAB POL optical microscope and JEOL JSM3600 scanning electron microscope were used for the micro-textural aspects of the study.

The grinding of the samples for XRD and XRF analyses was performed manually using a mortar and pestle to achieve fineness. After mineralogical characterization by XRD, the mineralogical quantification was performed by stoichiometry using chemical data determined by X-ray fluorescence (a SIEMENS SRS3000 spectrometer), by loss on ignition (LOI) and supported by thermogravimetric results. For the stoichiometry calculations the theoretical chemistry composition of the XRD-identified minerals was used: first by applying all the SiO_2 to kaolinite; then the remaining Al_2O_3 to gibbsite; any remaining LOI to goethite; finally, the hematite was quantified with the Fe_2O_3 after goethite; and the entire TiO_2 content was considered as anatase. In a sample of the nodular ferruginous horizon, the Rietveld quantified goethite content was considered as correct to enable the stoichiometric calculations. Mass loss from the different temperatures of dehydroxylation of the phases was also used to calculate gibbsite, kaolinite and goethite contents. For a precise stoichiometric content of goethite and hematite, their theoretical formula was calibrated after determination of their Al and Fe contents.

Approximately 10 mg of sample was heated in an alumina crucible using a heating rate of 10 K min^{-1} to perform thermogravimetric (TGA) and differential scanning calorimetry (DSC) in a thermal analyser NETZSCH STA 449 F3. The results were used to compare the mineral quantifications and determine temperatures of phase transitions.

Powder X-ray diffraction analysis for the Rietveld refinement was performed on an X´Pert Pro MPD (PW 3040/60) PANalytical diffractometer with Cu*K*α radiation and a Ni*K*β filter. The diffraction patterns were acquired from 5° to 70.00° (2θ) at 0.01° steps, a counting time of 20 s per step, resulting in a 20 mins measuring time. The mineralogical characterization and the Rietveld refinement were carried out with the PaNalytical software *HighScore Plus 4.5*, supported by the PDF4 + 2012 relational database. Crystal-structure data were obtained from the FIZ Karlsruhe database to which the CAPES foundation provided access. Rutile from KRONOS® 2900 was added to the material (0.4 g amounting to 20%) as an internal standard for the amorphous content quantification.

The refinement was performed with automatic background determination with granularity ≈20. The scale factors, the lattice parameters and the profile parameter W were constrained for almost all minerals in the first steps of the refinement. The preferred orientation of gibbsite (002) and kaolinite

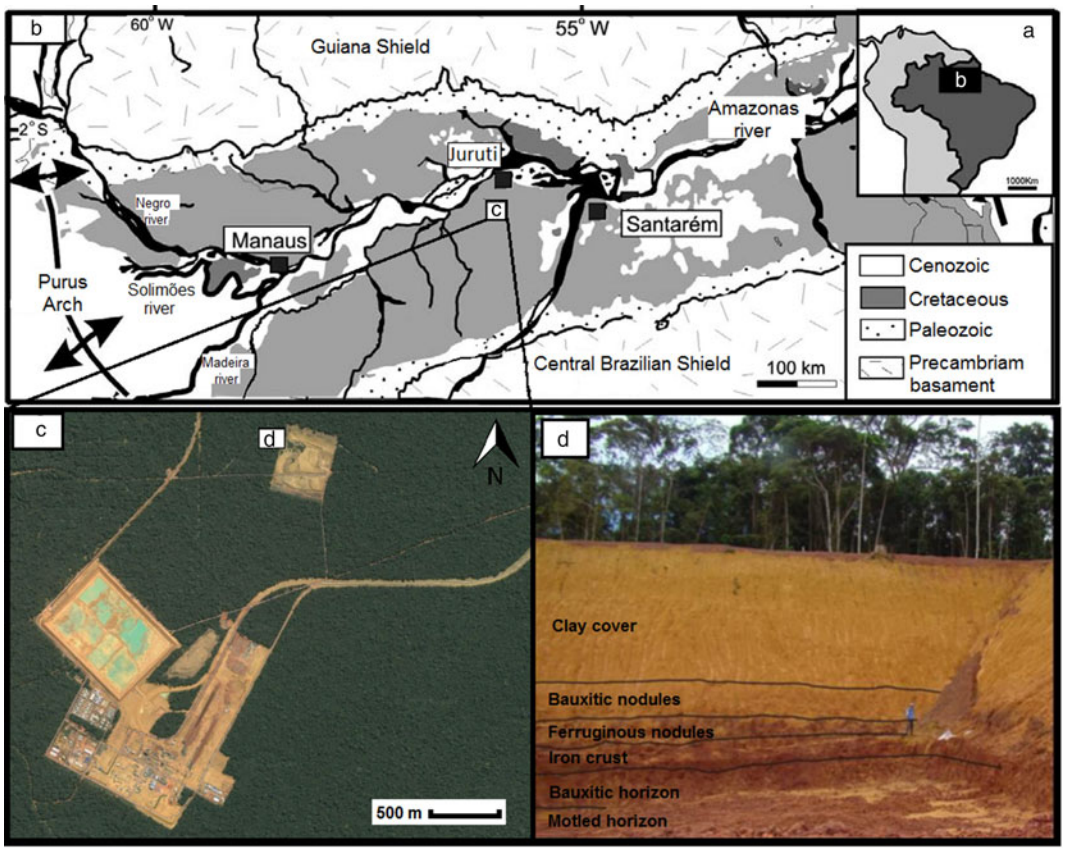

FIG. 1. (*a*) General location of the area studied; (*b*) geological sketch map of the Amazon Basin with location of the bauxite deposits in Juruti; (*c*) ALCOA bauxite mine facilities in Juruti; and (*d*) strip mining bank in the Capiranga plateau with exposition of different horizons of the bauxite-bearing regolith, in yellow the clay cover (Belterra clay). Modified from Mendes *et al.* (2012) and Cruz (2011).

(001) were refined for all the samples where these minerals represent the main phases.

Differences in intensity and even in some peak positions of the kaolinite in the clay cover compared to published structures of this mineral were broadly observed in the diffraction patterns. To perform a better profile fitting and quantification, a calibrated *hkl* phase model was produced for the kaolinites using the *Le Bail* fit method in the *HighScore 4.5* package. The unit cell and space group of the structure of kaolinite in the International Crystal Structure Database (ICSD) code 63192 was used in the *Le Bail* fit. The calibration of the *hkl* file was achieved using a carefully refined diffraction pattern of the clay cover, with its kaolinite content determined by stoichiometry. The obtained *hkl* calibrated file was used in the refinement of all other kaolinite-rich samples.

Further crystal-structure data used in the refinement include the ICSD codes 6162 for gibbsite (Saalfeld and Wedde, 1974), 109411 for goethite (Li *et al.*, 2006), 82137 for hematite (Sadykov *et al.*, 1996), 9853 for anatase (Horn *et al.*, 1972), 83710 for rutile (Howard *et al.*, 1991) and 83849 for quartz (Norby, 1997).

Results and discussion

Microscopy and micromorphology

Gibbsite occurs as the main phase in the bauxite-rich horizons (bauxite horizon and the horizon with bauxitic nodules) along the profile. It appears both in the fine matrix, associated with cryptocrystalline kaolinite and iron (oxy) hydroxide plasmas (Fig. 2) and, as well-shaped

prismatic and tabular crystals along fissures and filled microvoids (Fig. 2).

In the horizon with ferruginous nodules, remaining iron nodules are partially dissolved and involved with an external goethite cortex and 'meso-gibbsite' crystals in the inner part (Fig. 2). Those features associated with an Al-rich matrix with pores filled by gibbsite, indicate a partial aluminium remobilization through the regolith, probably associated with the dismantling of the

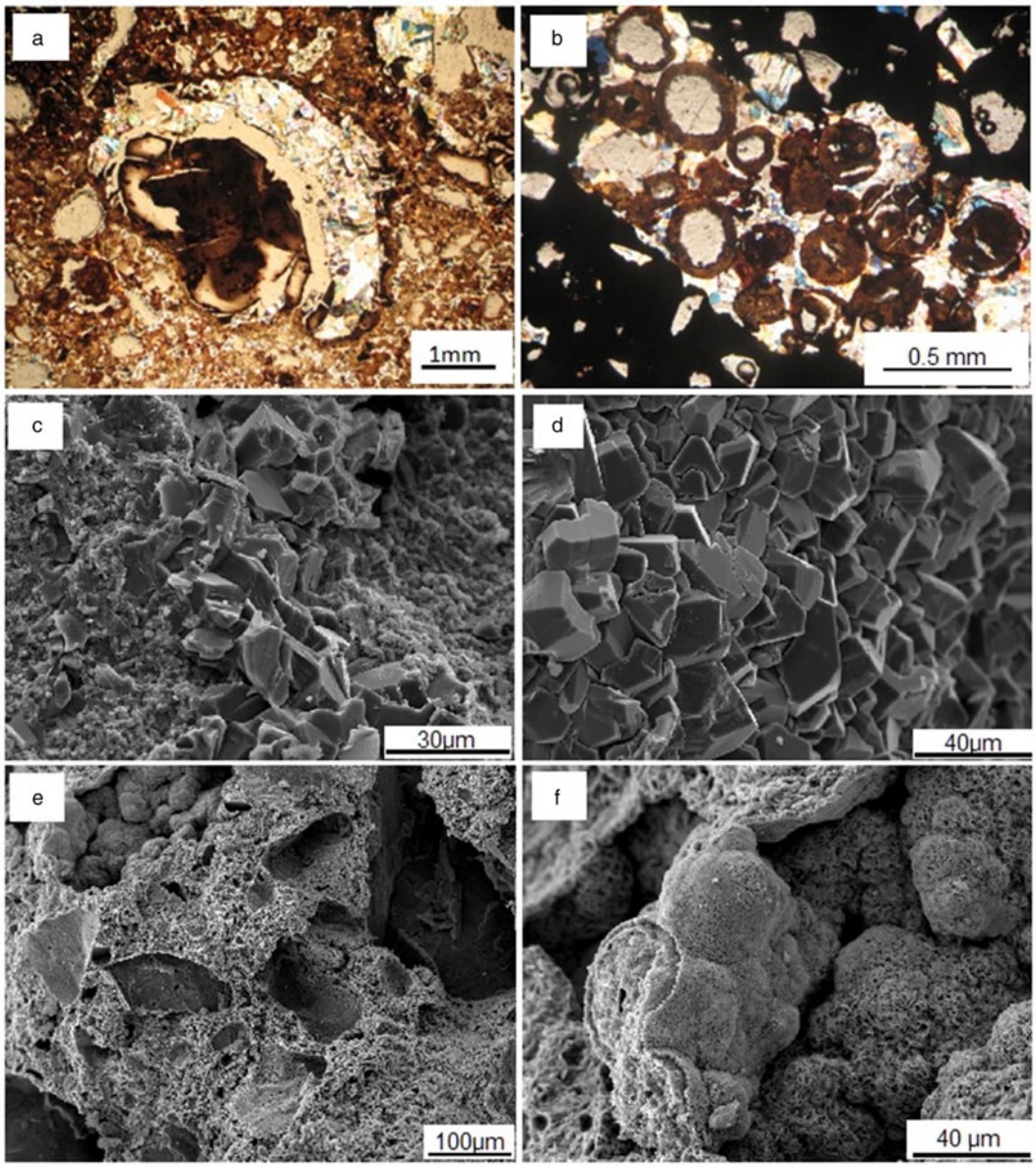

FIG. 2. Microtextural aspects of the bauxite-bearing regolith. (*a*) Dissolution pore filled by gibbsite in a cryptocrystalline aluminium-rich matrix; (*b*) dissolution pores filled by goethite and gibbsite in a dark hematite matrix; (*c*) and (*d*) bauxite micro-texture with well-shaped gibbsite crystals in the fine gibbsitic matrix; (*e*) detail of ferruginous nodules with pores; and (*f*) sub-spherical hematite aggregates.

iron crust as observed by Costa *et al.* (2014). As a result, a cavernous texture is observed under SEM where sub-spherical hematite crystal aggregates and prismatic well-formed gibbsite crystals occur inside many of the secondary dissolution pores (Fig. 2).

The kaolinite is present along all the horizons of the regolith, being the dominant phase in the clay horizon and the clayey overburden, where it is characterized predominantly as nano-crystalline, forming micro aggregates associated with goethite and nano-anatase (Costa *et al.,* 2014).

Chemical composition

The bulk chemical composition of the bauxite bearing regolith in Juruti (Table 1) is similar to most of the bauxite deposits in the Amazon. The bauxite has characteristic high contents of alumina and considerable silica due to the presence of kaolinite. Iron is the main constituent of the nodular ferruginous horizon, where substantial Al contents still remain. High contents of SiO_2 and Al_2O_3 in the clay cover are typical from Belterra clays of other localities, with a quasi-homogeneous composition, while TiO_2 contents increase gradually upwards through the profile.

Mineralogical composition by Rietveld refinement and stoichiometry

The Rietveld results displayed in Table 2 and compared with the stoichiometric calculations shows that gibbsite, kaolinite, goethite and hematite are the main minerals. Gibbsite is the major constituent of bauxite, being less frequent in the iron crust and its ferruginous nodules, and an accessory in the clay cover. Hematite and goethite are, as expected, the most abundant minerals of the iron crust and its dismantled products, while in the clay cover kaolinite and goethite prevail. According to XRD at least two generations of kaolinite can be recognized: a residual kaolinite and a newly-formed kaolinite that is very fine, nano-scale crystals and is concentrated in the clay cover.

The average of triplicate mineral quantification using Rietveld refinement of the complete profile, with Goodness-of-Fit (Goof) and *R*-weighted pattern (R_{WP}) values, followed by the stoichiometric results are shown in Table 2. Despite the good agreement obtained between the measured profile and the Rietveld calculated pattern (Figs 3 and 4), some peak overlaps influenced the performance of the calculations.

When compared to the stoichiometric calculation the most important difference was the amorphous phases. After the Rietveld refinement the bauxitic horizon consists predominantly of gibbsite (52.7%) and kaolinite (40%), with 2.6% hematite and 1.0% anatase. The calculated amorphous content reaches 3.6%.

In the nodular ferruginous horizon, hematite (55.8%) and gibbsite (19%) are the main minerals, with kaolinite reaching 16.3%, goethite 4.8% and anatase 0.95%. The calculated amorphous content is 2.35% indicating, according to the chemical analysis (Table 1), that the amorphous materials should be mostly iron (oxy)hydroxides.

The horizon with bauxitic nodules has gibbsite as the main phase representing 62.6% of the mineral content, whereas kaolinite reaches 28.4%, goethite 4.5% and anatase 1.4%. The amorphous content is 3.1%. According to the chemical analysis the amorphous material might consist of strongly disordered phases like aluminium hydroxides and hydrous aluminosilicates.

TABLE 1. Content of the major chemical element oxides (wt.%) and Loss on Ignition (LOI) in the bauxite-bearing regolith sequence of the Juruti mine.

	BX	NFH	NBH	CC 15.5 m	CC 9.5 m	CC 7.5 m	CC 3.0 m	CC 1.0 m
SiO_2	17.71	11.92	13.68	38.15	38.68	38.02	37.46	37.46
TiO_2	1.45	1.07	1.38	2.65	2.58	2.58	2.5	2.52
Al_2O_3	52.64	26.2	54.07	35.28	35.98	35.89	36.21	37.04
Fe_2O_3	2.73	46.2	3.28	7.98	7.5	7.63	6.96	7.11
LOI	25.38	14.16	27.44	15.67	15.05	15.65	16.65	15.64
Total	99.91	99.55	99.85	99.73	99.79	99.77	99.78	99.77

BX: bauxite; NFH: nodular ferruginous horizon; NBH: nodular bauxitic horizon; CC: clay cover.

TABLE 2. Average of the triplicate of all the mineral quantification by the Rietveld refinement (R) and stoichiometric (S) results along the regolith sequence.

Sample	Method	gibbsite	goethite	hematite	kaolinite	anatase	quartz	amorphous	Total	Goof	R_{wp}
BX	R	52.7	–	2.6	40.0	1.0	–	3.6	99.9	6.4	8.9
	S	57.3	–	2.9	38.1	1.5	–		100.0		
NFH	R	19.8	4.8	55.8	16.3	1.0	–	2.4	100.0	1.5	2.8
	S	20.2	4.8*	56.1	16.2	0.9	–		98.3		
NBH	R	62.6	4.5	–	28.4	1.4	–	3.1	100.1	3.1	8.4
	S	64.0	4.5	–	29.4	1.4	–		99.2		
CC 15.5	R	2.6	12.5	–	76.0	2.2	0.7	6.0	100.0	2.2	5.7
	S	2.8	11.1	–	80.0	2.7	1.0		97.7		
CC 13.5	R	1.3	11.7	–	81.9	2.7	0.5	1.9	100.0	2.2	5.8
	S	3.5	11.0	–	80.3	2.4	1.0		98.1		
CC 11.5	R	0.7	10.5	–	83.8	2.7	0.6	1.4	99.7	2.3	6.0
	S	3.4	10.7	–	80.1	2.6	1.0		97.8		
CC 7.5	R	0.8	12.2	–	83.0	2.0	0.4	1.4	99.9	2.3	6.0
	S	4.5	10.3	–	79.9	2.6	1.0		98.3		
CC 9.5	R	1.0	9.8	–	84.3	2.6	0.9	1.1	99.7	2.4	6.2
	S	4.0	10.7	–	79.7	2.6	1.0		98.0		
CC 5.0	R	1.9	11.2	–	80.0	2.2	0.5	4.4	100.2	2.4	6.3
	S	3.5	10.4	–	81.1	2.6	1.0		98.6		
CC 3.5	R	2.1	11.1	–	81.8	2.2	0.3	2.6	100.1	2.5	6.5
	S	5.1	9.8	–	78.9	2.5	1.0		97.2		
CC 3.0	R	2.1	11.0	–	80.1	2.2	0.2	4.4	100.0	2.5	6.4
	S	3.6	10.0	–	79.9	2.4	1.0		96.9		
CC 1.0	R	3.1	10.8	–	77.6	2.2	0.1	6.2	100.0	2.4	6.4
	S	5.6	9.7	–	78.5	2.5	1.0		97.3		
CC 0.5	R	3.3	10.9	–	78.2	2.1	0.2	5.3	100.1	2.4	6.4
	S	6.8	9.9	–	78.5	2.5	1.0		98.7		

BX: bauxite; NFH: nodular ferruginous horizon; NBH: nodular bauxitic horizon; CC: clay cover; Goof: Goodness of fit; R_{wp}: *R*-weighted profile. * – Rietveld calculated content for goethite.

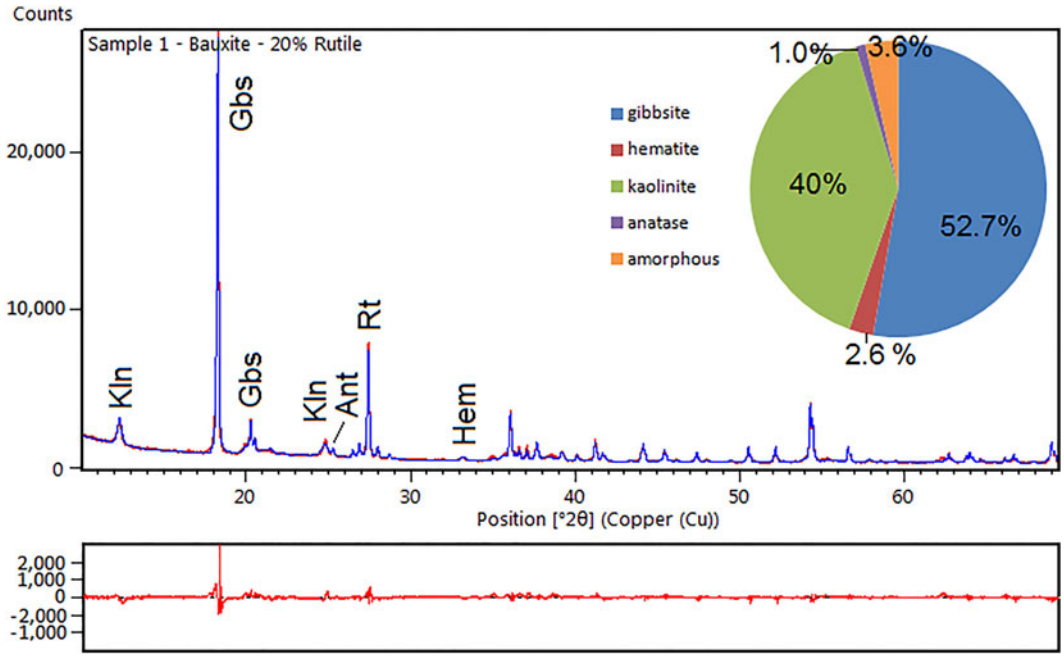

FIG. 3. XRD diagram and difference plot of a refined bauxite sample. Kln – kaolinite; Gbs – gibbsite; Ant – anatase; Rt – rutile (internal standard); and Hem – hematite.

With the greatest amounts of kaolinite (76.0–84.3%), the samples of the clay cover horizon were refined using an *hkl* model of kaolinite. The goethite and anatase contents are also higher in these samples, reaching 12.5% and 2.7%, respectively, whereas gibbsite occurs subordinately (up to 3.3%) and the amorphous contents range from 1.1 to 6.6%.

The statistical indicators Goof and R_{wp} are considered the best indices to evaluate the refinement (Toby, 2006) and are given in Table 2. The reproducibility of the method was tested by preparing, measuring and refining each sample in triplicate. The refined diffraction patterns show no significant discrepancies, attesting to good reproducibility of the method (Fig. 5).

DSC and TGA results

Fine gibbsite decomposes to χ-Al_2O_3 from temperatures of 270°C (Brindley and Choe, 1961), whereas goethite dehydroxylates around 300°C (Schulze and Schwertmann, 1984) and kaolinite at temperatures near to 500°C (Yeskis *et al.*, 1985). The thermal results of the bauxite sample shows two endothermic peaks in the DSC curve (Fig. 6), one at 299°C and the other at 496°C. They correspond to the decomposition of gibbsite and kaolinite, respectively. The associated mass loss of 19.71% and 5.99% may represent the dehydroxylation of these minerals. Using stoichiometrics these values represent 56.8% of gibbsite and 46% of kaolinite.

When compared to the bauxite sample, the bauxitic nodules also show, besides gibbsite and kaolinite dehydroxylations, goethite, which is represented by a small peak in the DSC curve at 360°C (Fig. 6). A mass loss of 0.67% accounts for the loss of water of goethite at this temperature and accounts for 6.0% of goethite in the sample, whereas the goethite quantified by the Rietveld method was 4.5%. The first loss of TGA curve (5.31%) is addressed to the decomposition of gibbsite and represents 61.3% of gibbsite in the sample, a value close to the quantified content by the Rietveld method (62.6%, Table 2).

The dehydroxylation of goethite is not observed as clearly in the sample of ferruginous nodules as in the other samples, but seems to be represented by a small shoulder in the DSC curve (Fig. 7) near to 400°C, overlapped by kaolinite, which dehydroxylates in this range of temperature, reaching its maximum at 487°C. As a deconvolution of

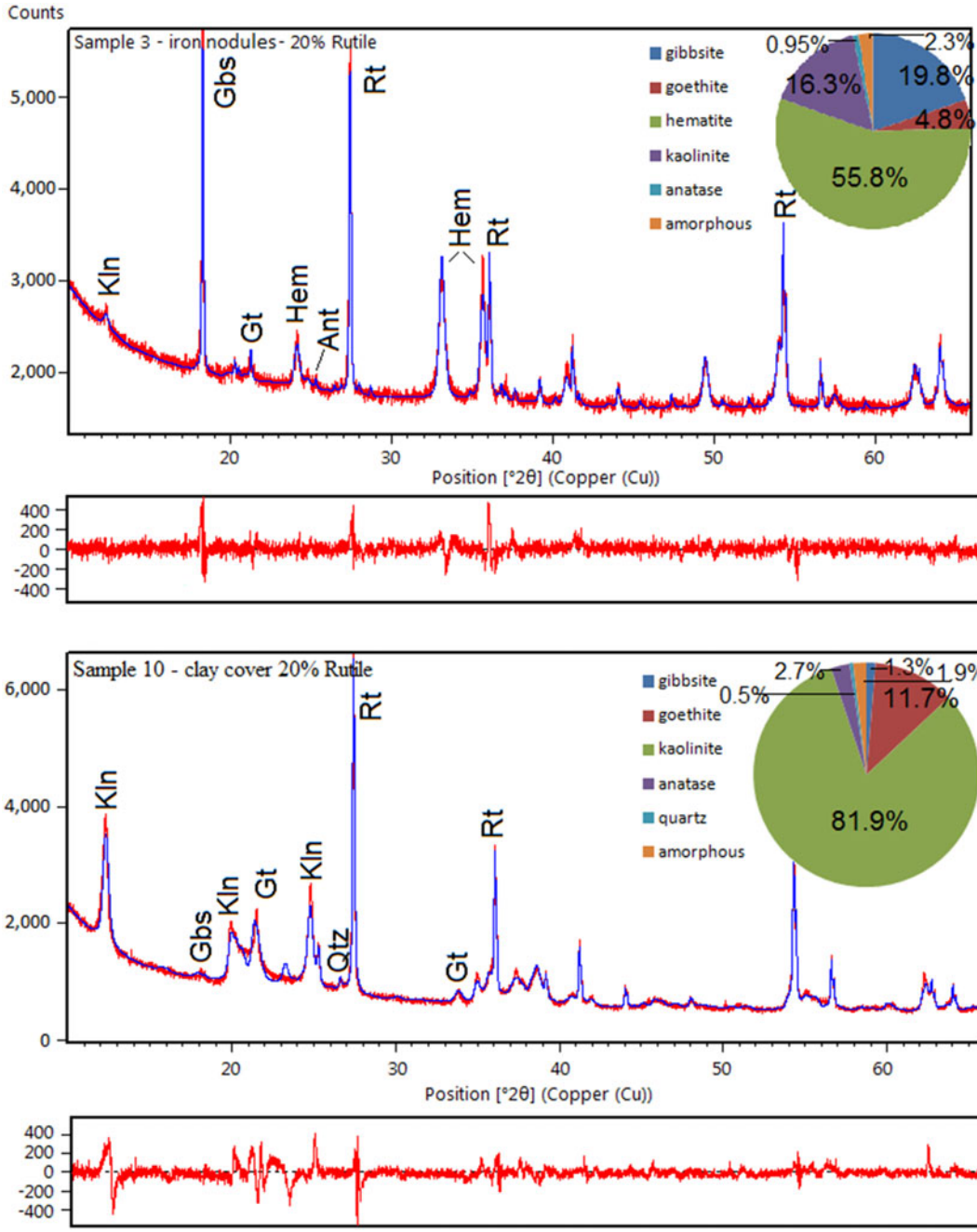

FIG. 4. XRD diagrams and difference plots of a refined pattern from the ferruginous nodules and a refined pattern from the clay cover. Kln – kaolinite; Gbs – gibbsite; Ant – anatase; Rt – rutile; Hem – hematite; Qtz – quartz; and Gt – goethite.

these peaks was not possible, the mass loss of 2.62% represents not only the kaolinite water, but also, partly, the goethite content.

When polycrystalline grains of coarsened gibbsite are heated, a water overpressure is developed in the inner part of these grains, forming an

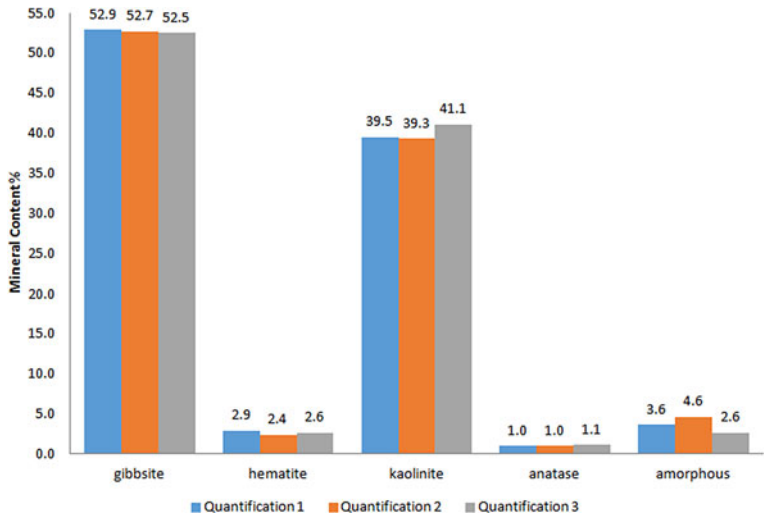

FIG. 5. Comparison of the results of the Rietveld refinement quantification in triplicate (Quantification 1, Quantification 2 and Quantification 3) for a bauxite sample.

environment close to hydrothermal conditions, transforming part of the gibbsite into poorly crystallized χ-Al_2O_3 and the inner part into bohemite (Mercury *et al.,* 2006). This results in two endothermic peaks: one around 230°C and other near 280°C, this latter endotherm is attributed commonly to the formation of boehmite (Colombo and Violante, 1996). Therefore, two small peaks at 235°C and 298°C in the DSC curve are related to the decomposition of gibbsite in a sample of the clay cover (Fig. 7). Another peak at 342°C represents the dehydroxylation of goethite with a loss of mass of 1.34%, which accounts for a calculated 12.0% of goethite in the sample, close to that obtained in the Rietveld refinement (11.7%). The kaolinite decomposition, and probably some böhmite, is represented by the peak with its maximum at 493°C.

Mineral chemistry

Goethite

Partial Al substitution for Fe in goethite is very common (Norrish and Taylor, 1961; Thiel, 1963; Schulze, 1984; Fazey *et al.*, 1991; Schwertmann and Carlson, 1994; Li *et al.*, 2006; Neumann *et al.*, 2014) and has been frequently described in lateritic profiles, including bauxite-bearing profiles (Fitzpatrick and Schwertmann, 1982; Trolard and Tardy, 1989; Kotschoubey *et al.*, 2005; Neumann *et al.*, 2014; Costa *et al.*, 2014). This corresponds to the partial solid solution goethite–diaspore and has the general formula $(Fe_{1-x}Al_x)OOH$, as proposed by Thiel (1963) for Al-rich goethites. These substitutions result in a linear shift of the d_{111}, d_{130}, d_{140} and d_{021} goethite peaks. Schulze (1984) described the linear decrease of the b lattice parameter related to the increasing substitution of Al-for-Fe (X_{Al}, in molar fraction) in synthetic goethites as:

$$X_{Al} = 17.30 - 5.72 \times b \quad (1)$$

Appling the Vegard's law with the b cell parameters of goethite, refined by the Rietveld method, the results suggest that this mineral in the Juruti regolith shows increasing Al content in the bauxite nodules (25.05 mol.%) and in the clay cover, ranging from 26.31% to 27.66 mol.%, below the maximum value of 36 (mol.%) determined by Schwertmann and Carlson (1994) in natural samples. The goethites are much less aluminous in the nodular ferruginous horizon, but still contain 10.46 mol% of Al.

Hematite

Hematite is also likely to have Al in their composition, forming a limited solid solution with corundum, as proposed by Stanjek and Schwertmann (1992). In contrast to goethite, the substitution of Al-for-Fe in hematite has no direct correlation with the lattice parameters, due to a coupled OH^- for O^{-2} substitution, resulting in the

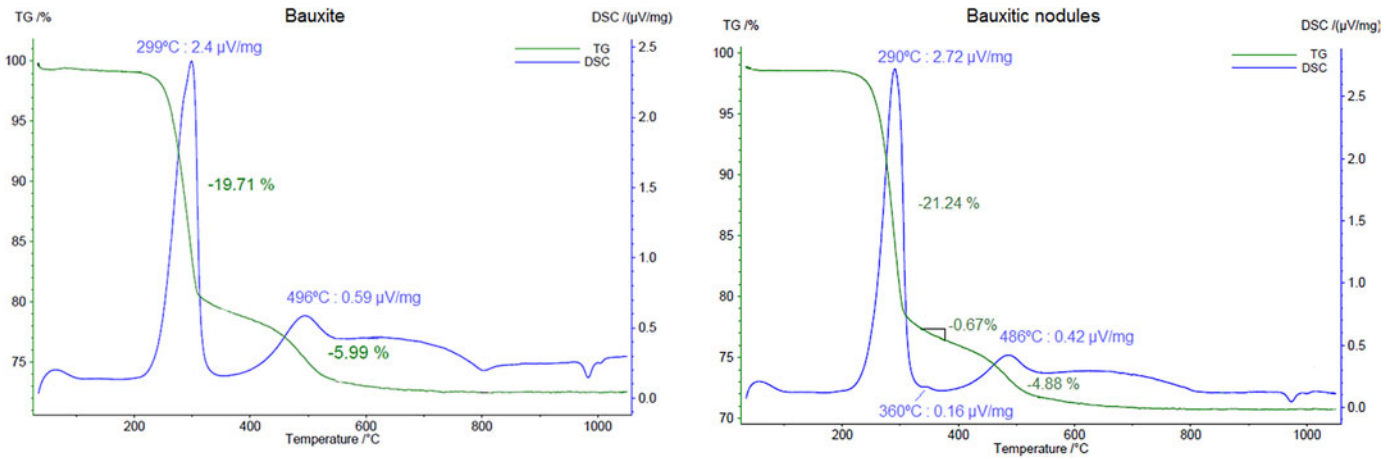

FIG. 6. TGA and DSC results of a sample of bauxite and a sample of the bauxitic nodules. Heating rate: 10 K min^{-1}.

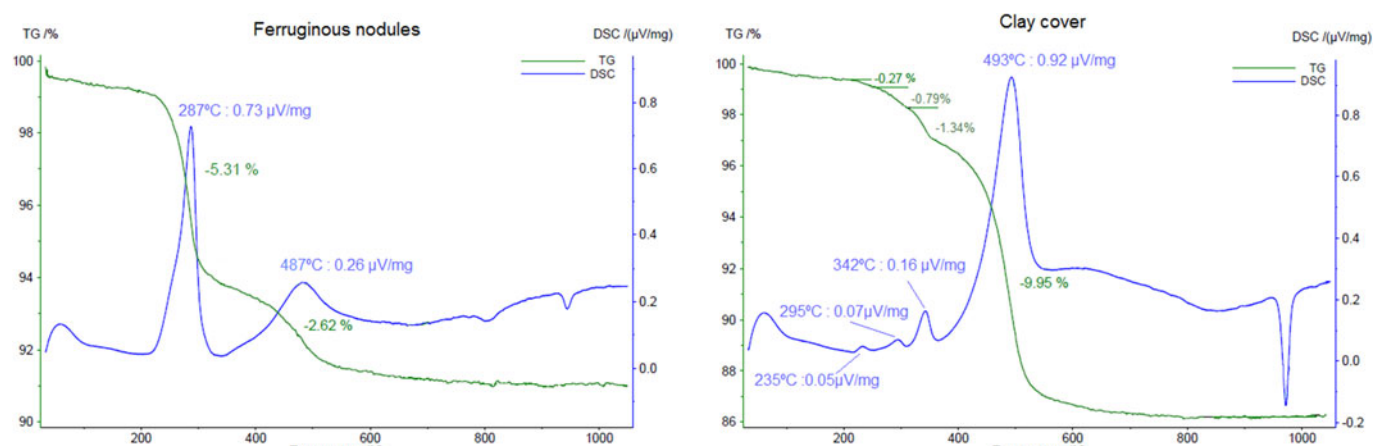

FIG. 7. TGA and DSC results for a sample the ferruginous nodules and a sample of the clay cover. Heating rate: 10 K min^{-1}.

TABLE 3. Al (mol.%) contents of the goethites along the regolith, calculated according to Schulze (1984).

Sample	*b* lattice parameter (Å)	Al (mol.%)
Clay cover 0.5 m	2.978	26.84
Clay cover 1.0 m	2.976	27.66
Clay cover 3.0 m	2.978	26.39
Clay cover 3.5 m	2.978	26.31
Clay cover 5.0 m	2.979	26.29
Clay cover 9.5 m	2.975	28.20
Clay cover 7.5 m	2.977	26.92
Clay cover 11.5 m	2.978	26.65
Clay cover 13.5 m	2.977	26.92
Clay cover (contact) 15.5 m	2.977	27.03
Nodular bauxitic horizon	2.981	25.05
Nodular ferruginous horizon	3.006	10.46

postulated general formula for the Al-rich hematite: $(Fe_{1-x}Al_x)_{2-z/3}(OH)_zO_{3-z}$. Stanjek and Schwertmann (1992) correlated the lattice parameters and the volume of the unit cell to the Al contents and the loss on ignition in synthesized hematite. Neumann *et al.* (2014) derived the equations from Stanjek and Schwertmann (1992) correlating the Fe, the Al and the OH occupancy (X_n, in molar fraction) to variation in the *a* and *c* lattice parameters of hematite:

$$X_{Fe} = (1 - (c - 13.7454)/0.72666) - (6019.83338 - 1518.37137a + 4.66753ac)/100 \quad (2)$$

$$X_{Al} = (6019.83338 - 1518.37137a + 4.66753a^2c)/100 \quad (3)$$

$$X_{OH}^{-} = (c - 13.7454)/0.24222 \quad (4)$$

The *a* and *c* lattice parameters of hematite obtained with the Rietveld refinement are presented in Table 4 together with the calculated Al, Fe and OH contents (in mol.%) from equations 2, 3 and 4, the vacancy at the Fe(Al) site and the OH^-/Al relation. According to the results, the hematites are characteristically less aluminous than goethites (Table 3), nonetheless hematites of the nodular ferruginous horizon and of the bauxite present 7.27 and 10.22 (mol.%) of Al, respectively, while the OH contents are 12.46 and 0.6 (mol.%).

The vacancies at the Fe(Al) site result from a compensation of charge imbalance due to the hydroxyl input, as the presented hematite formula requires ⅓ of the Fe(Al) position for each OH^--for-O^{-2} substitution (Neumann *et al.*, 2014). The increase in Al contents in hematite are thus associated with an increase in OH groups (Pinney and Morgan, 2013) and the OH/Al substitution ratio is close to 2.2, as averaged by Stanjek and Schwertmann (1992). Although most of the OH might surround the vacant Fe(Al) sites formed during hematite crystal growth (Cao *et al.*, 2015), Neumann *et al.* (2014) considered that loss of water by hematite crystals might be common during ageing of bauxites, providing low relations of OH/Al substitutions, similar to that presented in Table 4.

Kaolinite

Crystallinity indices for kaolinite such as the Hinckley Indices 'HI' (Hinckley, 1963), 'QF' of Range and Weiss (1969), 'R2' of Lièrtard (1977), 'IK' of Stoch (1974), 'H&B' of Hughes and Brown (1979) and the 'expert system' of Plançon and Zacharie (1990) could not be used in the samples of the regolith due to significant peak overlap in the observed XRD patterns. An alternative was the methodology proposed by Amigó *et al.* (1994), that only uses the (001) and (002) reflections of kaolinite that are not overlapped. Amigó *et al.* (1994) related the full width at half maximum (FWHM) of the (001) and (002) kaolinite reflections to their crystallinity. According to those

TABLE 4. Mineral composition of the hematites refined by the Rietveld method, calculated according to Stanjek and Schwertmann (1992).

Sample	*a* lattice parameter	*c* lattice parameter	Fe (mol.%)	Al (mol.%)	OH (mol.%)	Vacancy at Fe (Al) site	OH^-/Al
Nodular ferruginous horizon	5.032	13.774	88.67	7.27	12.46	0.04	1.7
Bauxite	5.027	13.760	87.73	10.22	6.29	0.02	0.6

authors, low FWHM are related to highly ordered kaolinites, whereas high FWHM values would represent less-ordered ones.

Using these relations, the kaolinite shows different crystallinity index values along the regolith (Fig. 8). The bauxitic horizon and the horizon with ferruginous nodules have the kaolinite with the highest order of the profile, whereas the horizon with bauxitic nodules and the clay cover have the lowest ordered ones. When compared to the study by Amigó *et al.* (1994), the kaolinite can be considered to have high to medium crystallinity.

The loss of order in kaolinite reflects the large number of stacking defects that may occur during

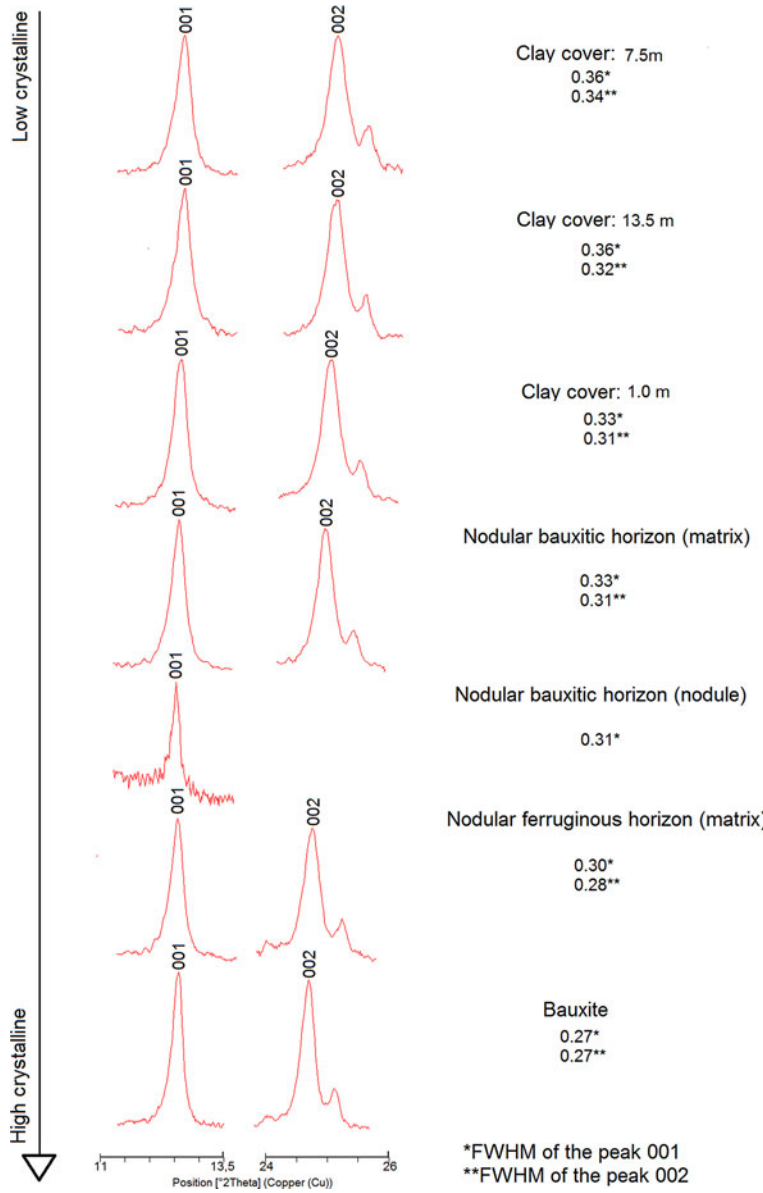

FIG. 8. Range of the kaolinite crystallinity (order) along the regolith sequence, calculated after Amigó *et al.* (1994). Clay Cover: 7.5 m (this number means depth) and so on.

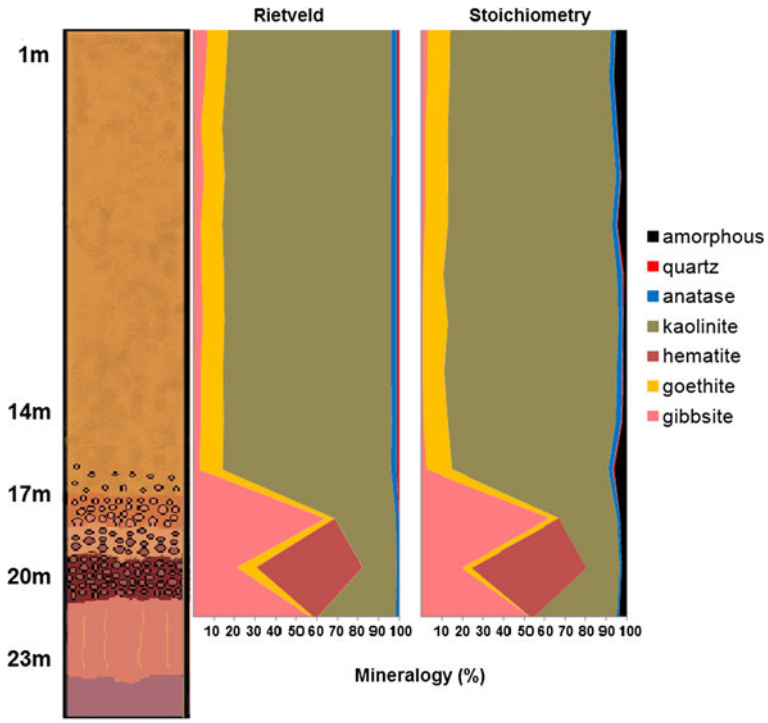

FIG. 9. Comparison between the mineral quantifications obtained by the Rietveld refinement and stoichiometry. For more details about lithology see Fig. 2.

the formation and growth of this mineral (Aparicio and Galán, 1999). These defects may also be influenced by the presence of Fe^{3+} in the Al (octahedral) position of kaolinite structures (Mestdagh *et al.*, 1980).

The results of the mineral quantification by stoichiometry and by the Rietveld refinement are very close (Table 2 and Fig. 9). The greatest difference is in the gibbsite contents, with lower values when quantified by the Rietveld method for almost all samples. Anatase is also frequently in disagreement with the stoichiometric results. Nevertheless the chemistry calculated after the Rietveld results also shows a good correspondence to the chemistry by stoichiometry using X-ray fluorescence, with the main differences in the Al_2O_3 and TiO_2 concentrations.

As observed by Paz *et al.* (2012), the principal differences between the diffraction patterns of kaolinite from the Amazon region and the diffraction patterns of published structures of this mineral are not in the peak positions, but in the relative intensity of the peaks. Therefore an *hkl* calibrated phase for kaolinite was used in the refinement. When observed by SEM the kaolinite are formed by nanometric sized (~200 nm) crystal aggregates, commonly associated with nano-anatase (Costa *et al.,* 2014).

Feret (2013) reported considerable amounts of amorphous material in bauxites, which may come from several sources simultaneously and labelled the result 'X-ray amorphous'. The author also used synchrotron radiation to obtain diffractograms that are sharper, more intense and with reduced background, allowing the partial identification of the so-called 'X-ray amorphous' phase. The quantified amorphous content for the samples studied can be high as 6.2% in a sample of the clay cover. In most samples with high contents of amorphous phases, gibbsite or kaolinite are underestimated when compared to stoichiometric results, suggesting this amorphous phase is related mainly to kaolinite, gibbsite or goethite that were not well solved in the refinement and therefore show up in the contents of 'X-ray amorphous'. Another possibility is that this material is in fact amorphous and possesses a similar chemical composition to these phases.

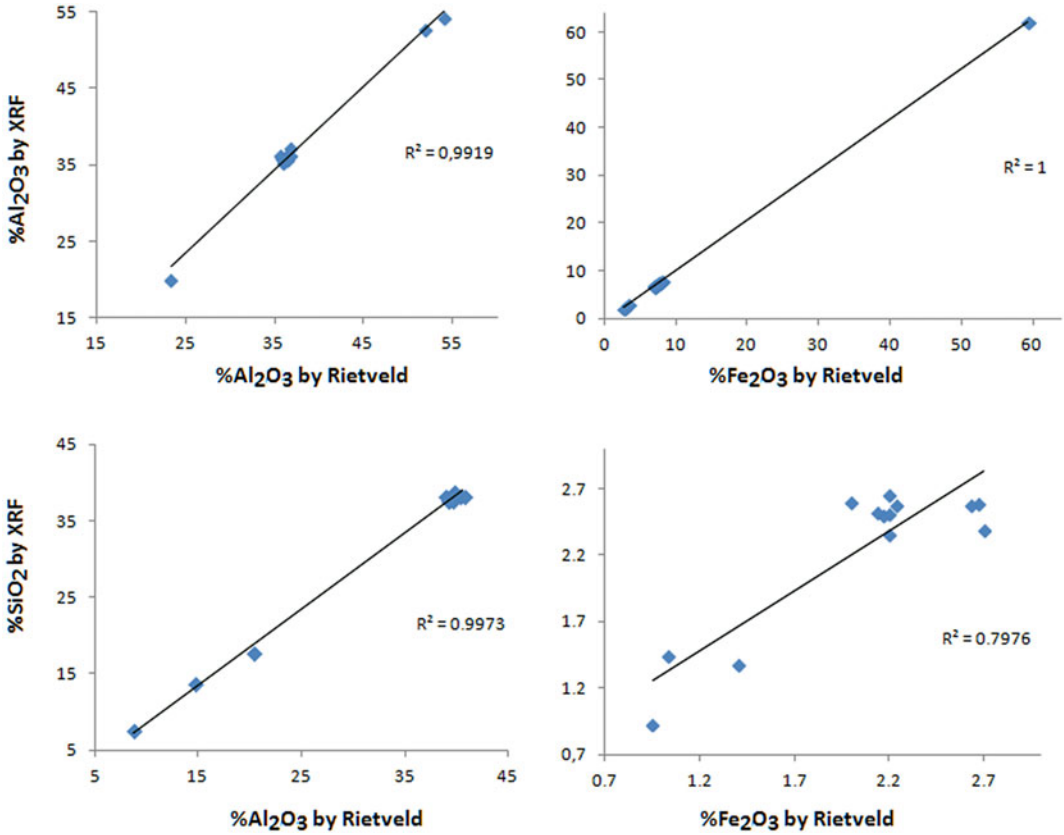

FIG. 10. Linear trend line of the chemical contents obtained by XRF and by Rietveld refinement.

The chemistry calculated after the Rietveld refinement (Fig. 10 and Table 5) shows that the quantified amorphous content does not have a chemical composition like kaolinite in the nodular ferruginous horizon, but is probably chemically similar to hematite and goethite. A probable contribution for the underestimation of hematite here might be related to the use of a Cu-anode, giving some fluorescence effect.

Along the Al-rich horizons of the regolith, aluminium plays a major role as the main chemical element constituent for gibbsite and kaolinite and also for replacing Fe in the crystal structures of goethite and hematite (Fig. 11 and Table 5). These substitutions reach up to 10.2% in hematite found in the bauxitic horizon and 28.2% in goethite found in the clay cover horizon. Fitzpatrick and Schwertmann (1982) observed significant negative correlations between the crystallinity of goethites and the substituted Al content, suggesting lower crystallinity for Al-rich goethites, which agrees with the generally not well-defined goethite peaks in the X-ray diffractograms.

The asymmetric shape of the 002 peak of gibbsite seems to be common in gibbsite-rich horizons of the regolith. König *et al.* (2012) observed a probable asymmetric pattern in other bauxites from the Amazon, and related the pattern to the presence of two generations of gibbsites, resulting in convoluted 002 peaks of the same mineral. After observation of gibbsites under the SEM, at least two generations were identified in the aluminium-rich horizons of the regolith, one coarser filling microvoids and another in the fine matrix. In addition to the different crystal size of these gibbsites, different crystallinities may also influence the XRD pattern. To solve the asymmetric peak problem due to the convoluted gibbsite peaks (Fig. 12), the crystallographic

TABLE 5. Content of the major chemical element oxides (wt.%) by mineral, along the regolith sequence, calculated using the Rietveld refinement.

	Al_2O_3gbs	Al_2O_3kln	Al_2O_3amf*	Al_2O_3gt	Al_2O_3hem	Al_2O_3tot	SiO_2kln	SiO_2qtz	SiO_2amf*	SiO_2tot	Fe_2O_3gt	Fe_2O_3hem	Fe_2O_3tot	TiO_2
BX	34.4	15.8	1.4	0.0	0.2	51.8	18.6	–	1.7	20.3	–	2.5	2.5	1.0
NFH	12.9	6.4	0.9	0.3	2.8	23.4	7.6	–	1.1	8.7	7.9	53.0	60.9	1.0
NBH	40.9	11.2	1.2	0.7	–	54.1	13.2	–	1.5	14.7	3.3	–	3.3	1.4
CC 15.5 m	1.7	30.0	2.4	1.9	–	36.0	35.4	0.7	2.8	38.9	8.0	–	8.0	2.2
CC 13.5 m	0.9	32.4	0.8	1.9	–	35.8	38.1	0.5	0.9	39.5	7.9	–	7.9	2.7
CC 11.5 m	0.5	33.1	0.6	1.8	–	35.9	39.0	0.6	0.7	40.3	7.7	–	7.7	2.7
CC 7.5 m	0.5	32.8	0.6	1.7	–	35.6	38.6	0.4	0.7	39.7	7.5	–	7.5	2.0
CC 9.5 m	0.7	33.3	0.4	1.9	–	36.3	39.3	0.9	0.5	40.6	7.7	–	7.7	2.6
CC 5.0 m	1.3	31.6	1.7	1.7	–	36.3	37.3	0.5	2.0	39.8	7.5	–	7.5	2.2
CC 3.5 m	1.4	32.3	1.0	1.6	–	36.3	38.1	0.3	1.2	39.6	7.1	–	7.1	2.2
CC 3.0 m	1.4	31.7	1.7	1.7	–	36.4	37.3	0.2	2.1	39.6	7.2	–	7.2	2.2
CC 1.0 m	2.0	30.7	2.4	1.6	–	36.7	36.1	0.1	2.9	39.1	7.0	–	7.0	2.2
CC 0.5 m	2.2	30.9	2.1	1.7	–	36.9	36.4	0.2	2.5	39.1	7.1	–	7.1	2.1

BX: bauxite; NFH: nodular ferruginous horizon; NBH: nodular bauxitic horizon; CC: clay cover. kln – kaolinite; qtz – quartz; amf* – amorphous considered as kaolinite; gbs – gibbsite; hem – hematite; gt – goethite; tot – total.

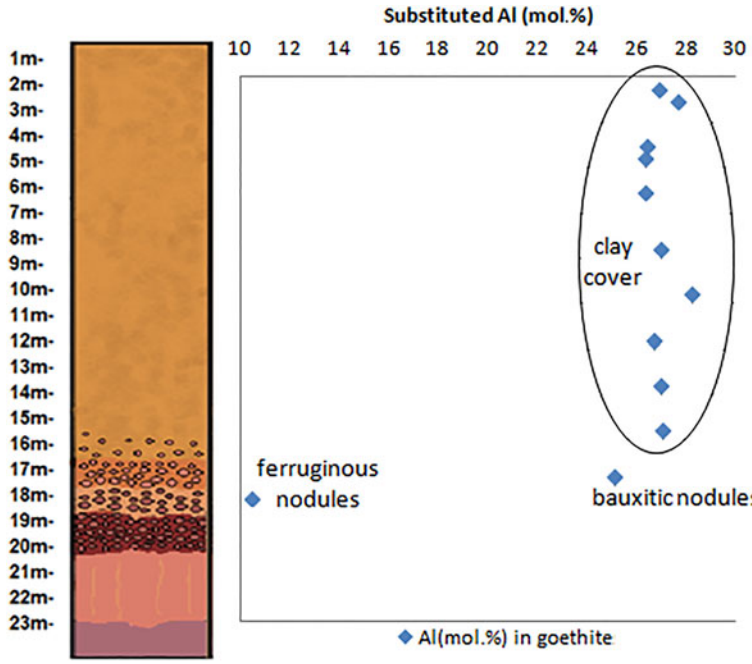

FIG. 11. Substituted Al (mol.%) contents in the hematites and goethites through the investigated regolith.

information file (cif) of this mineral was duplicated for a better fitting profile (Figs 3 and 4).

The quantified anatase contents by stoichiometry differ from those obtained by Rietveld refinement with a maximum overestimation of 30% in the clay cover and an underestimation of up to 50% in the bauxite sample, where TiO_2 content by XRF was 1.5% and the quantified anatase by Rietveld reaches up to 1.0%. As anatase is the main TiO_2 carrier (Costa *et al.*, 2014), the TiO_2 contents are considered as the real anatase contents. The overestimation obtained by the Rietveld refinement may occur due to flat background lines in kaolinite-rich samples, principally by the (101) anatase reflection, which occurs partially convoluted with the 002 peak of kaolinite, causing a slight

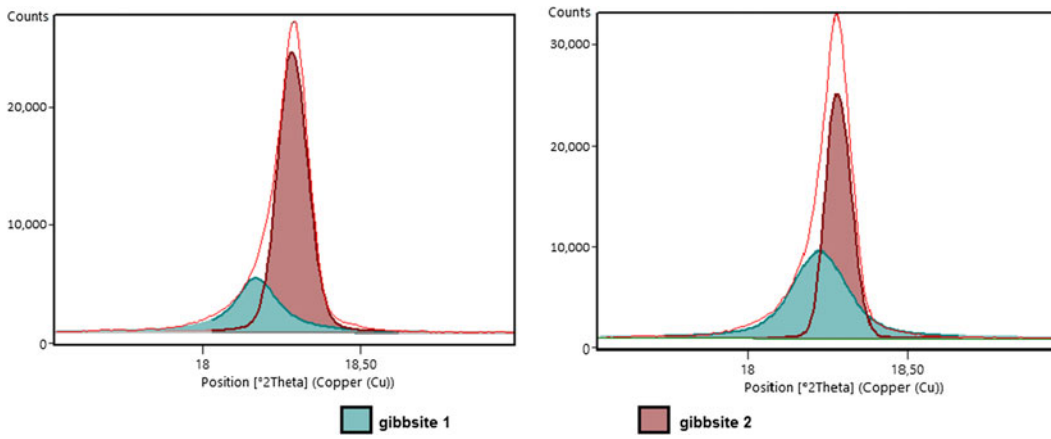

FIG. 12. Asymmetric (002) reflections of gibbsite reflecting the presence of two distinct generations of this mineral.

increase in the background, and difficulty with a precise background determination. The Rietveld refinement underestimations are mainly in samples with lower anatase and kaolinite contents, where the anatase peaks are smaller and frequently remain partially indistinguishable from the background, as in the ferruginous nodules.

Conclusions

Gibbsite, goethite, hematite, kaolinite and anatase are confirmed as typical mineral associations in lateritic profiles in the tropical region of the Amazon. The main mineral phases have variable concentrations and show different crystalline and chemical aspects along the regolith profile, as Al-rich goethite, kaolinite and partly Al-rich hematite. Compared with stoichiometric quantifications, the results were consistent, when the amorphous phase is considered as an amorphous analogue of kaolinite or gibbsite. With few exceptions, the thermal results are also in good accordance with the quantified mineralogy.

The *hkl* calibrated file used to refine kaolinite showed consistent results along the samples and was essential in the refinement as no proper crystal-structure data for this mineral are yet described. The reproducibility of the method showed accuracy for the dominant phases. For the subordinate minerals, the quantified contents show no significant differences. The discrepancy may occur due to a possible limitation of the method for phases with concentrations below 5%, but can be improved due to chemical analysis. The Goof and R_{wp} refinement indices indicate a satisfactory quality of refinement for this type of material with reproducible results. Rietveld refinement might be improved in the material by using synchrotron radiation for higher-resolution diffraction patterns.

Despite some minor limitations in the quantification of the bauxite-bearing regolith in Juriti, Brazil, the Rietveld refinement provides promising refined data, with importance at least in the bauxite exploration phase. These data can especially give important results due to its convenience, speed and quantification of the mineralogy of the phases.

Acknowledgements

The authors thank ALCOA for access to its Juruti bauxite mine and for allowing collection of samples along a complete profile. Financial support of the Brazilian National Research Council (CNPq) through research grants (Nr. 304.519/2009-0; 477.411/2012-6), the Science Without Borders program and the INCT – GEOCIAM/CNPq project is also gratefully acknowledged. The time consuming proof reading of the manuscript was undertaken by Prof. Ian Lerche.

References

Amigó, J.M., Batista, J., Sans, A., Signes, M. and Serrano, J. (1994) Crystallinity of Lower Cretaceous kaolinites of Teruel (Spain). *Applied Clay Science*, **9**, 51–69.

Aparicio, P. and Galán, E. (1999) Mineralogical interference on crystallinity index measurements. *Clays and Clay Minerals*, **47**, 12–27.

Bárdossy, G. and Aleva, G.J.J. (1990) *Lateritic Bauxites*. Developments in Economic Geology. Elsevier, Amsterdam, 624 pp.

Bray, E.L. (2016) *Bauxite and Alumina*. Mineral commodity summaries 2016, U.S. Geological Survey, Reston, Virginia, USA.

Brindley, G.W. and Choe, J.O. (1961) The reaction series, gibbsite → chi alumina → kappa alumina → corundum. *American Mineralogist*, **46**, 771–785.

Cao, S., Kang, F., Yang, X., Zhen, Z., Liu, H., Chen, R. and Wei, Y. (2015) Influence of Al substitution on magnetism and adsorption properties of hematite. *Journal of Solid State Chemistry*, **228**, 82–89.

Colombo, C. and Violante, A. (1996) Effect of time and temperature on the chemical composition and crystallization of mixed iron and aluminum species. *Clays and Clay Minerals*, **44**(1), 113–120.

Costa, M.L., Silva Cruz, G., Faria, H.F.A. and Pöllmann, H. (2014) On the geology, mineralogy and geochemistry of the bauxite-bearing regolith in the lower Amazon basin: Evidence of genetic relationships. *Journal of Geochemistry Exploration*, **146**, 58–74.

Cruz, G.S. (2011) *Bauxita, horizonte nodular e cobertura argilosa da região de Paragominas e Juruti, estado do Pará*. Dissertation, Universidade Federal do Pará, Brazil, 93 pp.

Fazey, P.G., O'Connor, B.H. and Hammond, L.C. (1991) X-ray powder diffraction characterization of synthetic aluminum substituted goethite. *Clays and Clay Minerals*, **39**, 248–253.

Feret, F.R. (2013) Selected applications of X-ray diffraction quantitative analysis for raw materials of the aluminum industry. *Powder Diffraction*, **8**, 112–123.

Fitzpatrick, R.W. and Schwertmann, U. (1982) Al-substituted goethite – an indicator of pedogenic and other weathering environments in South Africa. *Geoderma*, **27**, 335–347.

Hinckley, D.N. (1963) Variability in "crystallinity" values among the kaolin deposits of the coastal plain of Georgia and South Carolina. *Clays and Clay Minerals*, **11**, 229–235.

Horn, M., Schwerdtfeger, C.F. and Meagher, E.P. (1972) Refinement of the structure of anatase at several temperatures. *Zeitschrift für Kristallographie*, **136**, 273–81.

Howard, C.J., Sabine, T.M. and Dickson, F. (1991) Structural and thermal parameters for rutile and anatase. *Acta Crystallographica*, **47**, 462–468.

Hughes, J.C. and Brown, G. (1979) A crystallinity index for soil kaolins and its relation to parent rock, climate and soil nature. *Journal of Soil Scince*, **30**, 557–563.

König, U., Angélica, R.S., Norberg, N. and Gobbo, L. (2012) Rapid X-ray diffraction (XRD) for grade control of bauxites. *ICSOBA Proceedings*, **19**, 11pp.

Kotschoubey, B., Calaf, J.M.C, Lobato, A.C.C., Leite, A.S. and Azevedo, C.H.D. (2005) Caracterização e gênese dos depósitos de bauxita da Província Bauxitífera da Região de Paragominas, noroeste da Bacia do Grajaú, nordeste do Pará/oeste do Maranhão. Pp. 687–782 in: *Caracterização de Depósitos Minerais em Distritos Mineiros da Amazônia* (Marini, editors). DNPM – CT/ Mineral – ADIMB, Brasília.

Li, D., O'Connor, B.H., Low, I.M., van Riessen, A. and Toby, B.H. (2006) Mineralogy of Al-substituted goethites. *Powder Diffraction*, **21**, 289–299.

Lièvard, O. (1977) *Contribution à l'étude des Propiétés Phisicochimiques, Cristallographiques et Morphologiques des Kaolins*. PhD thesis, Nancy, France. 345 p.

Lucas, Y. (1997) The bauxite of Juruti. Pp 107–133 in: *Brazilian Bauxites* (A. Carvalho, editor). USP/ FAPESP/ORSTOM, São Paulo, Brazil.

Mendes, A.C., Truckenbrodt, W. and Nogueira, A.C. (2012) Análise faciológica da Formação Alter do Chão (Cretáceo, Bacia do Amazonas), próximo à cidade de Óbidos, Pará, Brasil. *Revista Brasileira de geociências*, **42**, 39–57.

Mercury, J.M., Pena, P., De Aza, A. H., Sheptyakov, D. and Turrillas, X. (2006) On the decomposition of synthetic gibbsite studied by neutron thermodiffractometry. *Journal of the American Ceramic Society*, **89**, 3728–3733.

Mestdagh, M.M., Vielvoye, L. and Herbillon, A.J. (1980) Iron in kaolinite: II. The relationship between kaolinite crystallinity and iron content. *Clay Minerals*, **15**, 1–12.

Neumann, R., Avelar, A.N. and Costa, G.M. (2014) Refinement of the isomorphic substitutions in goethite and hematite by the Rietveld method, and relevance to bauxite characterization and processing. *Minerals Engineering*, **55**, 80–86.

Norby, P. (1997) Synchrotron powder diffraction using imaging plates: crystal structure determination and Rietveld refinement. *Journal of Applied Crystallography*, **30**, 21–30.

Norrish, K. and Taylor, R.M. (1961) The isomorphous replacement of iron by aluminum in soil goethites. *Journal of Soil Science*, **12**, 294–306.

Oliveira, S.B., Costa, M.L. and Prazeres Filho, H. (2016) The lateritic bauxite deposit of Rondon do Pará: A new giant deposit in the Amazon region, Northern Brazil. *Economic Geology*, **111**, 1277–1290.

Paz, S.P.A., Angélica, R.S. and Scheller, T. (2012) X-ray diffraction studies of kaolinites to support mineralogical quantification of high silica bauxites from the Brazilian Amazon region. *ICSOBA Proceedings*, **19**, 1–7.

Plançon, A. and Zacharie, C. (1990) An expert system for the structural characterization of kaolinites. *Clay Minerals*, **25**, 249–260.

Pinney, N. and Morgan, D. (2013) *Ab initio* study of structurally bound water at cation vacancy sites in Fe- and Al-oxyhydroxide materials. *Geochimica et Cosmochimica Acta*, **114**, 94–111.

Range, K.J. and Weiss, A. (1969) Über das Verhalten von Kaoliniti bei hohen Drücken. *Berichte der Deutschen Keramischen Gesellschaft*, **46**, 231–288.

Rietveld, H.M. (1969) A profile refinement method for nuclear and magnetic structures. *Journal of Applied Crystallography*, **2**, 65–71.

Saalfeld, H. and Wedde, M. (1974) Refinement of the crystal structure of gibbsite, $Al(OH)_3$. *Zeitschrift für Kristallographie*, **139**, 129–135.

Sadykov, V.A., Isupova, L.A., Tsybulya, S.V., Cherepanova, S.V., Litvak, G.S., Burgina, E.B., Kustova, G.N., Kolomiichuk, V.N., Ivanov, V.P., Paukshtis, E.A., Golovin, A.V. and Avvakumov, E.G. (1996) Effect of mechanical activation on the real structure and reactivity of iron (III) oxide with corundum-type structure. *Journal of Solid State Chemistry*, **123**, 191–202.

Schulze, D.G. (1984) The influence of aluminum on iron oxides. VIII. Unit-cell dimensions of Al-substituted goethites and estimation of Al from them. *Clays and Clay Minerals*, **32**, 36–44.

Schulze, D.G. and Schwertmann, U. (1984) The influence of aluminium on iron oxides: X Properties of Al- substituted goethites. *Clay Minerals*, **19**, 521–539.

Schwertmann, U. and Carlson, L. (1994) Aluminum influence on iron oxides: XVII. Unit-Cell parameters and aluminum substitution of natural goethites. *Soil Science Society of America Journal*, **58**, 256–261.

Silva, A.P.J., Lopes, R.C., Vasconcelos, A.M. and Bahia, R.B.C. (2003) Bacias Sedimentares Paleozóicas e Meso-cenozóicas Interiores. Pp. 53–85 in: *Geologia, Tectônica e Recursos Minerais do Brasil* (Bizzi, editors). CPRM, Brasília.

Sombroek, W.G. (1966) *Amazon Soils. A Reconnaissance of the Soils of the Brazilian Amazon Region*. Centre for Agricultural Publications and Documentation, Wageningen, The Netherlands, 292 pp.

Stanjek, H. and Schwertmann, U. (1992) The influence of aluminum on iron oxides: Part XVI,

Hydroxyl and aluminum substitution in synthetic hematites. *Clays and Clay Minerals*, **40**, 347–354.

Stoch, L. (1974) *Mineraly Ilaste* ("Clay Minerals"). Geological Publishers, Warsaw [pp 186–193].

Thiel, R. (1963) Zum System a-FeOOH-a-AlOOH. *Zeitschrift für anorganische und allgemeine Chemie*, **326**, 70–78.

Trolard, F. and Tardy, Y. (1989) A model of Fe(3+) kaolinite, Al(3+)-Goethite, Al(3+)-Hematite equilibria in laterites. *Clay Minerals*, **24**, 1–21.

Toby, H.B. (2006) R factors in Rietveld analysis: How good is good enough? *Powder Diffraction*, **21**, 67–70.

Yeskis, D., Koster van Groos, A. and Guggenheim, S. (1985) The dehydroxylation of kaolinite. *American Mineralogist*, **70**, 159–164.